**The Cryosphere
Discussions**

Mass balance of the Greenland ice sheet – a study of ICESat data, surface density and firn compaction modelling

L. S. Sørensen[1,2,*]**, S. B. Simonsen**[3,4,*]**, K. Nielsen**[5]**, P. Lucas-Picher**[4]**, G. Spada**[6]**,
G. Adalgeirsdottir**[4]**, R. Forsberg**[1]**, and C. S. Hvidberg**[3]

[1]Geodynamics Department, DTU Space, Juliane Maries vej 30, 2100 Copenhagen, Denmark
[2]Planet and Geophysics, NBI, University of Copenhagen, Juliane Maries Vej 30,
2100 Copenhagen, Denmark
[3]Centre for Ice and Climate, NBI, University of Copenhagen, Juliane Maries Vej 30,
2100 Copenhagen, Denmark
[4]Danish Climate Centre, DMI, Lyngbyvej 100, 2100 Copenhagen, Denmark
[5]Geodesy Department, DTU Space, Juliane Maries vej 30, 2100 Copenhagen, Denmark

[6]Dept. of Mathematics, Informatics, Physics, and Chemistry, Urbino University "Carlo Bo",
Via Santa Chiara, 27, 61029 Urbino (PU), Italy
[*]These authors contributed equally to this work.

Correspondence to: L. S. Sørensen (slss@space.dtu.dk)
and S. B. Simonsen (sbs@nbi.ku.dk)

Abstract

ICESat has provided surface elevation measurements of the ice sheets since the launch in January 2003, resulting in a unique data set for monitoring the changes of the cryosphere. Here we present a novel method for determining the mass balance of the Greenland ice sheet derived from ICESat altimetry data.

Four different methods for deriving the elevation changes from the ICESat altimetry data set are used. This multi method approach gives an understanding of the complexity associated with deriving elevation changes from the ICESat altimetry data set.

The altimetry can not stand alone in estimating the mass balance of the Greenland ice sheet. We find firn dynamics and surface densities to be important factors in deriving the mass loss from remote sensing altimetry. The volume change derived from ICESat data is corrected for firn compaction, vertical bedrock movement and an intercampaign elevation bias in the ICESat data. Subsequently, the corrected volume change is converted into mass change by surface density modelling. The firn compaction and density models are driven by a dynamically downscaled simulation of the HIRHAM5 regional climate model using ERA-Interim reanalysis lateral boundary conditions.

We find an annual mass loss of the Greenland ice sheet of $210 \pm 21\,\mathrm{Gt\,yr^{-1}}$ in the period from October 2003 to March 2008. This result is in good agreement with other studies of the Greenland ice sheet mass balance, based on different remote sensing techniques.

1 Introduction

Different satellite based measuring techniques have been used to observe the present-day changes of the Greenland ice sheet (GrIS). Synthetic Aperture Radar (SAR) imaging reveals an acceleration of a large number of outlet glaciers in Greenland (Abdalati et al., 2001; Rignot et al., 2004; Rignot and Kanagaratnam, 2006; Joughin et al., 2010).

Gravity changes observed by the Gravity Recovery And Climate Experiment (GRACE) show a significant mass loss (Velicogna and Wahr, 2005; Luthcke et al., 2006; Wouters et al., 2008; Sørensen and Forsberg, 2010; Wu et al., 2010). Local elevation changes of the GrIS with significant thinning along the ice margin are revealed by laser altimetry (Slobbe et al., 2008; Howat et al., 2008; Pritchard et al., 2009).

We provide a novel mass balance estimate of the GrIS for the period 2003–2008, derived from elevation measurements from NASA's Ice, Cloud, and land Elevation Satellite (ICESat), firn compaction and surface density modelling.

Different methods have been used to derive secular surface elevation change estimates $\left(\frac{\mathrm{d}H}{\mathrm{d}t}\right)$ of snow or ice covered areas from ICESat data (Fricker and Padman, 2006; Howat et al., 2008; Slobbe et al., 2008; Pritchard et al., 2009). Here we use four different methods to derive $\frac{\mathrm{d}H}{\mathrm{d}t}$, and the differences are investigated.

The total volume change of the GrIS is found by fitting a smooth surface, which covers the entire ice sheet, to the ICESat derived $\frac{\mathrm{d}H}{\mathrm{d}t}$ estimates. The conversion of the derived $\frac{\mathrm{d}H}{\mathrm{d}t}$ values to mass changes is based on firn compaction and surface density modelling, forced by climate parameters from a regional climate model (RCM). Other studies have linked climate models and surface mass balance models in order to estimate the mass balance of the GrIS (Li et al., 2007; van den Broeke et al., 2009), but in our approach we directly use the estimated $\frac{\mathrm{d}H}{\mathrm{d}t}$ values from ICESat to derive the total mass balance including firn dynamics, driven by the HIRHAM5 high resolution RCM. The HIRHAM5 simulation is a dynamical downscaling of the ECMWF ERA-Interim reanalysis (Sect. 5.2).

The first part of this paper is dedicated to the description of the ICESat data and the methods used for deriving elevation and volume changes of the GrIS (Sects. 2 to 3). The volume change estimates and their associated uncertainties are presented in Sect. 4.

In the second part of this paper, the volume to mass conversion is described (Sects. 5 to 7). This includes the changes in the firn compaction and surface density of the GrIS. The theoretical treatment of the firn dynamics involved in elevation changes without

contributing to the mass balance of the GrIS is presented in Sect. 5. The findings from both observations and model treatment are combined to derive the total mass balance of the GrIS in Sect. 7.

2 ICESat data

ICESat carries the Geoscience Laser Altimeter System (GLAS) instrument (Abshire et al., 2005). Technical problems with the GLAS instrument early in the mission have resulted in a significant reduction in repeated tracks, and hence in spatial resolution. Successive tracks are separated by approximately 30 km in the southern part of Greenland, because the GLAS instrument has been operating only 2–3 months per year.

The GLAS/ICESat Antarctic and Greenland Ice Sheet Altimetry Data product (GLA12) (Zwally et al., 2010) was downloaded from the National Snow and Ice Data Center. This level-2 altimetry product provides geolocated and time tagged ice sheet surface elevation estimates, with respect to the TOPEX/Poseidon reference ellipsoid. The satellite laser footprint size is 30–70 m and the distance between the footprint centers is approximately 170 m. This study is based on the 91-day repeat cycle ICESat data (release 31) from October 2003 to March 2008. The time span and release number of the laser campaigns in the data set are listed in Table 1.

2.1 ICESat data pre-processing

A procedure of data culling and application of corrections is necessary to reduce some of the systematic errors in the ICESat data set, and to remove problematic measurements (Smith et al., 2005). Saturation of the waveform can induce errors in surface elevation estimates (Fricker et al., 2005). Applying the saturation correction to the relevant measurements, which are flagged in the data files, reduces these errors (NSIDC, 2010). We have also used the difference between the shape of the return signal and a Gaussian fit (the IceSvar parameter), to evaluate data. Large differences indicate

2107

less reliable surface elevation estimates, and measurements for which the misfit is large (IceSvar ≥ 0.04 V) are rejected from the further analysis. Multiple peaks can be caused by reflections from clouds. All measurements that contain more than one peak in the return signal are rejected from the analysis. Besides these two criteria, we have also used data quality flags and warnings given with the data to reject problematic measurements. We find that these thresholds result in a satisfactory size of crossover error.

Only measurements from the GrIS and the surrounding glaciers and ice caps are considered in the elevation change analysis. The total number of ICESat measurements from the ice covered areas is 10 367 807. After rejecting problematic measurements in the data culling procedure, the number is reduced by approximately 13% to 9 053 639. The details are listed in in Table 1.

3 Methods for deriving surface elevation changes

The individual ICESat tracks are not precisely repeated but can be up to several hundred meters apart. Thus the observed elevation difference between tracks contains contributions from terrain, seasonal variations and secular trends.

The fact that the ICESat tracks are not exactly repeated, complicates the methods for deriving $\frac{dH}{dt}$ along-track, due to the presence of a cross-track slope, caused by the topography. The cross-track slope must be determined and subtracted in order to derive the actual elevation change. Several methods for doing this have previously been published (Fricker and Padman, 2006; Howat et al., 2008; Slobbe et al., 2008; Pritchard et al., 2009). We present $\frac{dH}{dt}$ results obtained by using four different methods (M1–M4). The methods have different strengths and weaknesses, which become apparent when comparing the results. M1–M3 are along-track analysis and are all set up to estimate $\frac{dH}{dt}$ at a 500 m along-track resolution. M4 is a crossover analysis, and hence the spatial resolution obtained by this method is lower. An observed elevation difference between tracks will also include a seasonal signal, caused by variations in accumulation, flow

2108

and melt during the year. In all four approaches we solve for both a secular trend $\frac{dH}{dt}$ and a seasonal signal, $s(t)$. Hence, the time dependent surface elevation, $\tilde{H}(t)$, is parameterised as:

$$\tilde{H}(t) = \left(\frac{dH}{dt}\right)t + s(t),\tag{1}$$

where the seasonal signal is given by:

$$s(t) = D\cos\left(\frac{2\pi}{T}t + \phi\right) = \alpha\cos(\omega t) + \beta\sin(\omega t),\tag{2}$$

with amplitude $D = \sqrt{\alpha^2 + \beta^2}$, period T (365 days), and a phase ϕ.

Each of the $\frac{dH}{dt}$ estimates from the four methods are associated with a variance from the regression procedure applied. $\frac{dH}{dt}$ values associated with a large variance are not used in the mass balance calculation.

3.1 Method 1

In principle, a Digital Elevation Model (DEM) could be used to correct for the surface slope, and this approach is used in the first method (M1). Unfortunately there are no independent, sufficiently accurate high resolution DEM's available which cover the entire GrIS. Following Slobbe et al. (2008), we choose the DEM generated from the first campaigns of ICESat data (DiMarzio et al., 2007). The grid spacing of this DEM is 1 km and the elevations are given relative to the WGS 84 ellipsoid.

In order to subtract the DEM from the ICESat data, the DEM is linearly interpolated to estimate the value in each data location. The height of each ICESat measurement above the reference DEM is given by:

$$\Delta H^{M1} = H^{ICESat} - H^{DEM},\tag{3}$$

where H^{ICESat} is translated into elevations above the WGS84 ellipsoid, to be comparable with the DEM elevations (H^{DEM}).

The measurements are catagorized according to the ICESat track (i) and 500 m along-track segment denoted j. The mean of the ΔH^{M1} values of each ICESat campaigns is calculated in each segment, creating time series of $\Delta \bar{H}^{M1}$ values along-track.

$$\Delta \bar{H}_{ij}^{M1} = \begin{pmatrix} A_{ij} \\ B_{ij} \\ \alpha_{ij} \\ \beta_{ij} \end{pmatrix} (\bar{t}, 1, \cos\omega t, \sin\omega t),\tag{4}$$

where $A_{ij} = \left(\frac{dH}{dt}\right)_{ij}$, B_{ij} is the offset between the DEM and the ICESat elevations in the segment, and $\bar{t}$ is the mean time of a campaign in a given segment.

The governing equation, Eq. (4) is solved using ordinary least squares regression.

Only the long wavelength component of the terrain slope is removed, due to the relative low resolution of the DEM, compared to the spacing of the ICESat along-track measurements. The 1 km resolution is too low to capture the true topography in some areas, and this will most likely be reflected in the elevation changes calculated using this method.

3.2 Method 2

The second method (M2) is similar to the one presented by Pritchard et al. (2009). In each of the along-track segments, a reference surface is created from elevation measurements from two ICESat campaigns. The reference surface is represented by a centroid point (x_0, y_0, H_0) and slopes $\left(\frac{dH}{dx}, \frac{dH}{dy}\right)$. The choice of the two campaigns which are used to generate the reference surface is based on two criteria. The first criterium is that the two campaigns are separated by one year in time. This ensures that both the seasonal signal and the actual change in elevation between the two are minimized. The second criterium is the ICESat tracks used to generate the reference surface, are the ones that span the largest area. These criteria help to ensure that the reference surface is representative of the surface slope. Hence, it is considered the

reference for all other ICESat measurements in a given along-track segment, similar to the use of a DEM in M1:

$$\Delta H^{\mathrm{M2}} = H^{\mathrm{ICESat}} - H^{\mathrm{ref}},$$ (5)

The height of the reference surface in a point (x, y) is given by:

$$H_{ij}^{\mathrm{ref}} = \left(\frac{\mathrm{d}H}{\mathrm{d}x}\right)_{ij}(x - x_0) + \left(\frac{\mathrm{d}H}{\mathrm{d}y}\right)_{ij}(y - y_0) + H_0.$$ (6)

The approach of solving for $\frac{\mathrm{d}H}{\mathrm{d}t}$ is similar to Eq. (4).

In spite of the criteria used to select the ICESat campaigns from which the reference surface is generated, method M2 is sensitive to seasonal variations and actual elevation changes between the two campaigns chosen. The $\frac{\mathrm{d}H}{\mathrm{d}t}$ estimates will therefore be biased.

3.3 Method 3

The third method (M3) is similar to the one presented in Howat et al. (2008) and Smith et al. (2009). In each along-track segment, the surface elevation H^{M3} is assumed to vary linearly with position (x, y), time (t) and a sine and cosine term, describing the seasonal signal:

$$H_{ij}^{\mathrm{M3}} = \begin{pmatrix} A_{ij} \\ B_{ij} \\ \alpha_{ij} \\ \beta_{ij} \\ \left(\frac{\mathrm{d}H}{\mathrm{d}x}\right)_{ij} \\ \left(\frac{\mathrm{d}H}{\mathrm{d}y}\right)_{ij} \end{pmatrix} \left(\bar{t}, 1, \cos \omega t, \sin \omega t, (x - x_0), (y - y_0)\right),$$ (7)

where $A_{ij} = \left(\frac{\mathrm{d}H}{\mathrm{d}t}\right)_{ij}$, $\left(\frac{\mathrm{d}H}{\mathrm{d}x}\right)$ is the along-track slope, $\left(\frac{\mathrm{d}H}{\mathrm{d}y}\right)$ is the cross-track slope, and B_{ij} is an estimate of the topography underlying the elevation changes. (x_0, y_0) is the

2111

centroid point of the area spanned by all of the measurements in the track segment. In each segment, a least squares linear regression is performed to estimate the elevation change.

This method is sensitive to track geometry, since the method assumes that the H dependence in x, y and t is independent. For certain track constellations this will certainly not be the case.

3.4 Method 4

In the fourth method (M4), elevation changes are estimated only at crossover locations. From the ICESat data set (2003–2008), we find 458 432 crossovers.

The surface elevation at a track crossover location is found by linear interpolation of the closest points on the two tracks, located at each side of the crossover. In order to secure a fair estimate of the elevation at the crossover, a crossover is rejected if the north-south distance between the two closest points are grater than 500 m. This rejection criterium results in a subset of approximately 266 701 crossovers accepted for further analysis.

In contrary to the other three methods M1–M3, the elevation change at the crossover locations only contains the seasonal signal and the actual change in elevation. The elevation change is estimated in the crossover location of track n and m by a simple least squares linear regression.

$$\Delta H_{nm}^{\mathrm{M4}} = A_{nm}\Delta t_{nm} + s_{nm}(t) + B_{nm},$$ (8)

where $\Delta H_{nm}^{\mathrm{M4}}$ contains the elevation differences between track n and m, and Δt_{nm} contains the corresponding time differences. $A_{nm} = \left(\frac{\mathrm{d}H}{\mathrm{d}t}\right)_{nm}$ is the estimated elevation change in the location of the crossover between track n and m, $s_{nm}(t)$ is the seasonal signal and B_{nm} is the offset.

The disadvantage of this method is the poor spatial coverage of elevation change results, especially in the southern part of Greenland.

2112

3.5 Elevation change results

The elevation changes obtained by the four methods show that there is a good agreement between the patterns of elevation changes (see Fig. 1a–d). A distinct thinning of the ice sheet is generally found along the southeast and west coast, while a smaller but consistent thickening is found in the interior part of the ice sheet, which is in agreement with other altimetry studies (Abdalati et al., 2001; Thomas et al., 2008, 2009; Slobbe et al., 2008; Pritchard et al., 2009). On the more local scale, the thickening of Flade Isblink (81.4° N, 15.1° W) and Storstrømmen (77.1° N, 22.6° W) are identified by all methods.

A fixed threshold of $6\,\text{m}^2$ for the variance associated with the fit of the regression is applied, and the number of output values from each method is an indication of how well a given method performs. The number of $\frac{dH}{dt}$ estimates with variance below the threshold is 264 635 for M1, 257 241 for M2, 276 717 for M3, and 4457 for M4.

This result indicates that M3 is preferable, since the largest number of accepted output values is obtained with this method.

4 Deriving volume changes

In order to estimate the total annual volume change, a smooth surface is fitted through the $\frac{dH}{dt}$ estimates, which covers the entire ice sheet. For this purpose ordinary kriging is used. The uncertainty in the total volume change is quantified using a bootstrap method.

4.1 Interpolation of volume changes

The $\frac{dH}{dt}$ estimates are interpolated onto a 5×5 km grid, using ordinary kriging. For all 4 method results, an exponential variogram model with a practical range of 150 km has been used. The range and the choice of model are based on the experimental

2113

variogram. Due to the large number of the $\frac{dH}{dt}$ estimates, local neighborhood kriging is used. Cross validation analysis is applied in order to determine the sufficient number of closest points to be used in the interpolation. In order to pass on the variances from the regression analysis, from which the elevation changes are determined, these have been added to the variogram model (Pebesma, 1996). The R package gstat has been used for the kriging procedure (Pebesma, 2004).

The estimated volume changes are summarized in Table 2. The estimates are of little significance without knowing their associated uncertainties. It is often difficult analytically to keep track of the error when different calculations have been performed on data, and therefore a bootstrap method (Davison and Hinkley, 2006) is used to quantify the uncertainty.

4.2 Bootstrapping

Bootstrap is a resampling method (Davison and Hinkley, 2006). The basic idea of this method can be explained by the following steps.

(1) Create a resample by drawing random samples with replacements from an original data set, where it is assumed that the observations are independent. In this way a new data set is obtained with the same length as the original data set.

(2) Estimate the wanted parameter from the resample, in this case the annual volume change.

(3) Repeat step 1 and 2 N times.

These estimates represents a distribution of the wanted parameter, from which information of the uncertainty can be obtained.

Here, the original data set is the set of $\frac{dH}{dt}$ estimates. For each method 1000 resamples are created, from which an error estimate can be found. For method M1, M2, and M3 a resample is made by sampling between entire tracks contrary to individual

2114

$\frac{dH}{dt}$ values, since these are highly correlated along-track. In method M4 the $\frac{dH}{dt}$ values are independent at the crossover locations, hence a resample is made by sampling between the $\frac{dH}{dt}$ values.

4.3 Volume change results

The 1000 bootstrap resamples make up the distributions of the volume changes. For all methods these distributions are approximately normally distributed and centered around the point estimate of the volume change (see Fig. 2). Hence the 95% confidence interval of the volume change will be $\pm 2\sigma$, where σ is the standard deviation. The error estimates of the volume changes are summarized in Table 2.

There is a relatively large spread in the resulting volume changes. In order to determine which method gives the best estimate, the four methods must be reevaluated.

Method M4 gives the smallest volume change estimate of $-147 \pm 24\,\text{km}^3\,\text{yr}^{-1}$. This was expected since the density of crossovers is clearly under-represented in the southern part of Greenland (see Fig. 1) where the largest thinning is found, and many of the outlet glaciers in these regions will then not be captured correctly. We believe that the volume estimate found from M2 of $-179 \pm 15\,\text{km}^3\,\text{yr}^{-1}$ is also an under-estimation. It is likely that the reference surface, which is created in M2, contains an actual elevation change, and this will result in biased $\frac{dH}{dt}$ values. The fact that M2 most likely dampens the signal of areas with large elevation changes, is also reflected in the relatively low standard deviation of the bootstrap procedure. The volume change results from methods M1 and M3 are similar, with volume change estimates of $-225 \pm 23\,\text{km}^3\,\text{yr}^{-1}$ and $-237 \pm 25\,\text{km}^3\,\text{yr}^{-1}$, respectively. We find that a larger number of accepted $\frac{dH}{dt}$ are obtained from M3 than M1, see Sect. 3.5, and that the M1 estimates are associated with larger variances than those of M3. Furthermore, it is seen in Fig. 2 that the M1 distribution is wider than the M3 distribution.

From the above argumentation it is concluded that method M3 gives the most reliable estimate of the volume change.

2115

5 Modelling firn compaction and surface densities

Firn compaction and surface density of the ice sheet must be taken into account, in order to relate the ICESat measurements of changes in surface elevation to mass changes. The firn compaction responds dynamically to changes in surface temperature and precipitation. This dynamic response will not contribute to the mass balance of the GrIS, and therefore it is subtracted from the observed elevation change before converting it into mass change.

In general the change in surface elevation can be parameterised by

$$\frac{dH}{dt} = \frac{\dot{b}}{\rho} + w_c + w_{ice} + \frac{\dot{b}_m}{\rho} + w_{br} - u_s\frac{dS}{dx} - u_b\frac{dB}{dx}\,, \tag{9}$$

where $\dot{b}$ is the surface mass balance, ρ is the density of the snow or ice, w_c is the vertical velocity of the surface due to the changes in firn compaction, in the following referred to as the firn compaction velocity. w_{ice} is the vertical velocity of the ice matrix, $\dot{b}_m$ is the basal mass balance, w_{br} is the vertical velocity of the underlying bedrock associated with glacio-isostatic adjustment, u_s is the horizontal ice velocity of the surface, S, and u_b is the horizontal velocity of the ice at the bed B (Paterson, 2002; Zwally and Li, 2002; Helsen et al., 2008). A cartesian coordinate system with a vertical axis pointing upwards is used and we define accumulation positive and ablation negative. Changes in w_{ice} can be neglected over short time spans (Zwally and Li, 2002) and $\dot{b}_m$, $u_s\frac{dS}{dx}$ and $u_b\frac{dB}{dx}$ are assumed to be constant. Thus, over the short time span of the ICESat measurement Eq. (9) can be used to express the rate of mass change of the GrIS, derived from observations of the elevation change,

$$\dot{b} = \left(\frac{dH^{ICESat}}{dt} - w_c - w_{br}\right)\rho\,, \tag{10}$$

where $\frac{dH^{ICESat}}{dt}$ is the estimated elevation change observed from ICESat altimetry. w_c

2116

and ρ can only be estimated from models of the firn compaction and density and w_{br} is estimated in accordance to Sect. 6.1.

5.1 Firn compaction model

In order to estimate the effect of firn compaction on short time scales, a time-dependent densification model is needed. Following Reeh (2008), the time-dependent contribution to the elevation change from changes in firn compaction is the sum of annual firn layer anomalies with respect to a steady state reference. The steady state reference is defined as the youngest layer in the firn column which is unaffected by the inter-annual variability in the surface temperature and surface mass balance. The firn compaction velocity is then defined as

$$w_c = \frac{1}{\Delta t} \sum_{t_2=0}^{t-t_0} \sum_{t_i=0}^{t-t_0-t_2} \left(\lambda(t_0 + t_2, t_0 + t_i) - \lambda_{ref}(t_0 + t_i) \right), \tag{11}$$

where t_0 is the time of deposition, $\lambda(t_0, t)$ is the annual layer thickness at a time $t = t_0 + t_i$ after deposition, and λ_{ref} is the steady state reference. $\lambda(t_0, t)$ depends on the local mass balance and is given by

$$\lambda(t_0, t) = \begin{cases} \left(\frac{(b(t_0) - r(t_0))\rho_i}{\rho_f(t_0, t)} + r(t_0) \right) \tau \,, & \text{if } b(t_0) \geq 0 \\ b(t_0)\delta(t - t_0)\tau & , \text{if } b(t_0) < 0 \end{cases}, \tag{12}$$

where $r(t_0)$ is the amount of refrozen melt water, ρ_i is the density of ice, τ is a time constant usually equivalent to one year and δ is the Kronecker delta function (Reeh et al., 2005). The firn density $\rho_f(t_0, t)$ can be derived from the Zwally and Li (2002) parameterisation of the Herron and Langway (1980) densification model

$$\rho_f(t_0, t) = \begin{cases} \rho_i - (\rho_i - \rho_s(t_0))\exp(-ct_i) & , \text{if } \rho_f(t_0, t) \leq \rho_c \\ \rho_i - (\rho_i - \rho_c)\exp(-c(t_i - t_c)) & , \text{if } \rho_f(t_0, t) > \rho_c \end{cases} \tag{13}$$

2117

where ρ_c is the critical firn density of $550\,\text{kg/m}^3$ defined by Herron and Langway (1980), t_c is the time it takes for the firn to reach the critical density, and c is the densification constant describing the linear change in air volume in the firn due to the overlaying pressure (Reeh, 2008). The Zwally and Li parameterisation differs from the original Herron and Langway densification model by the parameterisation of c, where the Zwally and Li parameterisation is more sensitive to the temperature (Reeh, 2008). This sensitivity is important when evaluating changes in firn compaction on short time scales.

The densification constant is given by

$$c = \frac{b(t)\rho_i}{\rho_w}\beta(T)K_G(T), \tag{14}$$

where $\beta(T)$ is a scale factor accounting for changes in grain growth with temperature T and ρ_w is the density of water. K_G is the rate factor for densification adjusted for grain growth

$$K_G = K_{0_G}\exp\left(\frac{E(T)}{RT}\right) = 8.36T^{-2.061} \tag{15}$$

Here, K_{0_G} is the rate factor only for grain growth, E is the activation energy and R is the gas constant (Zwally and Li, 2002; Reeh, 2008). The effect of grain growth (β) was assumed to be eight by (Zwally and Li, 2002). Later empirical studies reported a site dependency of β between seven and three (Li et al., 2003) at sites with an annual mean temperature between -30 and $-22\,°C$. We assume $\beta = 8$, since this study covers the entire GrIS, where annual mean temperature is exceeding temperatures of $-22\,°C$ in some areas.

5.2 HIRHAM5 – forcing of the firn compaction model

The annual mean temperature at two meter above the surface, runoff, snowfall and precipitation variables, required for the firn compaction model, are produced by dynamically downscaling the European Centre for Medium-Range Weather Forecast

2118

(ECMWF) ERA-Interim reanalysis with the HIRHAM5 regional climate model (RCM). The HIRHAM5 RCM (Christensen et al., 2006) is a hydrostatic RCM developed at the Danish Meteorological Institute (DMI). It is based on the HIRLAM7 dynamics (Eerola, 2006) and ECHAM5 physics (Roeckner et al., 2003). The ERA-Interim reanalysis (Simmons et al., 2007), provided by the ECMWF, is a comprehensive reanalysis of the state of the atmosphere, using measurements from satellite, weather balloons and ground stations.

A continuous simulation with HIRHAM5 at 0.05 deg. ($\sim$5.55 km) resolution on a rotated grid is realized from 1989–2008 using the ECMWF ERA-Interim at T255 ($\sim$0.7° or $\sim$77 km) as lateral boundary conditions. The sea-surface temperature and sea-ice distribution, taken from ERA-Interim, were interpolated to the HIRHAM5 grid and prescribed to the model. The wind components, atmospheric temperature, specific humidity and surface pressure from ERA-Interim were transmitted to HIRHAM5 every six hours for each atmospheric model level of the HIRHAM5 RCM. At the lateral boundaries of the model domain, a relaxation scheme according to Davies (1976) is applied with a buffer zone of ten grid boxes. The high 5.5 km horizontal resolution data are appropriate to determine the precipitation distribution over the sharp edge of the ice sheet, where the ablation zone is located. The dynamical downscaling with a RCM allows to simulate climate variables, which are physically consistent, for every grid cell of the domain.

A comparison of the publicly available 1.5° × 1.5° ERA-Interim and the HIRHAM5 dynamical downscaling are shown in Fig. 3. It is clear how the high resolution HIRHAM5 RCM run is able to account for the complex coastal topography in Greenland. The coastal precipitation patterns propagate far inland to areas above the equilibrium line altitude (ELA), where the firn compaction is applied. This pattern is not captured by the ERA-Interim (see Fig. 3) and shows the need for the high resolution RCM's input to the firn compaction modelling.

5.3 Interpolated metric grid

In order to derive the mass change of the GrIS the area of each grid box has to be known. To ensure equal area of each grid box the high resolution data from the HIRHAM5 RCM is interpolated onto the equal distance 5 × 5 km grid by a nearest neighbor interpolation. The snowfall of 2008 in the two different map projections is shown in Fig. 3. It is seen that the pattern of snowfall is preserved after the grid transformation. However, the interpolation becomes noisier the greater the distance is to the equator of the original HIRHAM map projection. The noise is seen in the high precipitation area near Station Nord in the Northeastern Greenland. Despite the noise induced by the transformation of map projections, the equal distance grid gives a good approximation of the precipitation and temperature field over the GrIS produced by the HIRHAM5 model. We will use the HIRHAM5 on the equal distance grid, to force the surface density and firn compaction.

5.4 Refreezing of melt water and formation of ice lenses

On the GrIS, 60% of the run-off given by the HIRHAM5 RCM is assumed to refreeze in the snowpack (Reeh, 1991). The accumulation is calculated as the sum of snowfall and the refrozen run-off. To simplify the following derivation of a time dependent densification model the refrozen run-off is assumed to refreeze inside the annual layer in the firn, from which it originates, and the water is not allowed to penetrate deeper into the firn column. This assumption is in violation with observations from the Arctic snowpack where melt water is often seen to penetrate the snowpack until it reaches a hard layer where the melt water flows along until it refreezes or finds a crack to propagate downwards into the deeper firn (Benson, 1962; Bøggild, 2000; Jansson et al., 2003). In order to be able to model this behavior, sub-annual layering of the densification model and knowledge of grain growth in water-saturated firn would be required. Both of these are outside the scope of the present study of firn compaction, where the overburden

pressure is believed to be the driving force, despite the fact that melt water percolation may redistribute the load on a layer.

5.5 Results of firn compaction and density modelling

The density of the snow/ice involved in the mass change of the GrIS in Eq. (10), is modeled in order to derive the mass change of the GrIS from the ICESat measurements. The density is assumed to be either the density of ice or firn, depending on the location on the ice sheet. The density of the surface firn is highly dependent on the temperature during the precipitation event.

In the ablation zone, defined here for simplification as the area below the ELA, all elevation change is assumed to be caused by ice. Above the ELA, in the accumulation zone, an elevation increase is assumed to be caused by an addition of snow/firn. However, an elevation decrease is assumed to be caused by the remote removal of ice in the ablation zone as a response to ice dynamics. The surface density is then parameterised by

$$\rho = \begin{cases} \rho_s \text{ , if } \frac{dH}{dt} \geq 0 \text{ and H } \geq \text{ELA} \\ \rho_i \text{ , else} \end{cases}, \tag{16}$$

where ρ_s is the surface density of firn including ice lenses, and is given by

$$\rho_s = \frac{\rho_0}{1 - \frac{r}{b}\left(1 - \frac{\rho_0}{\rho_i}\right)} . \tag{17}$$

Here, r is the amount refrozen melt water inside an annual firn layer, $\rho_i = 900 \text{ kg m}^{-3}$ and ρ_0 is the temperature dependent density of new firn before formation of ice lenses

$$\rho_0 = 625 + 18.7T + 0.293T^2 \tag{18}$$

(Reeh et al., 2005). T is the temperature given in °C. The ELA is determined using the polynomial parameterisation described by Box et al. (2004), where the ELA is given by

a 2nd order polynomial in West Greenland and a 5th order polynomial in East Greenland as a function of the latitude.

Based on the HIRHAM5 climatology for the period 1989 to 2008, the annual firn layer thickness has been computed according to Eq. (12). To derive the firn compaction velocity from Eq. (11) a steady state reference (λ_{ref}) has to be defined. The time span of the climate record is too short to define a robust steady state reference for the firn compaction. Moreover, the inter-annual variation in temperature and precipitation will bias a chosen reference to the climate pattern that is dominant in the time span of the reference period. To avoid defining the steady state reference layer thickness we have chosen to compare the thickness of the top firn layers in the period from 2003 to 2008. The maximum number of layers, which can be evaluated in 2003, is 15. Hence the thickness of the top 15 layers is compared from year to year in the period 2003 to 2008 at each grid point above the ELA. The change in the thickness is seen in Fig. 4a, along with the error in the linear fit in Fig. 4d. The change in the thickness of the 15 layers is a combination of changes in accumulation/surface melt and changes in the firn compaction. The change in the accumulation given in ice equivalent for the top 15 layer thickness is seen in Fig. 4b. By subtracting the change in the thickness of the 15 layers in ice equivalent from the 15 layer firn thickness, the change in air volume of the top firn, is found. The rate of change in this air volume in the firn is equivalent to the firn compaction velocity defined in Eq. (11). The approach of evaluating the relative change in air volume in each grid point above the ELA avoids the definition of a steady state reference for the firn compaction. The resulting firn compaction velocity is the linear trend in air volume of the top 15 layers for period 2003 to 2008, and is depicted in Fig. 4c. The error in the linear fit is seen Fig. 4f.

In Fig. 4c it is seen how the firn compaction velocity is mainly increasing in the central area of the GrIS, whereas, the firn in the coastal areas is becoming more dense. This pattern shows the importance of taking the firn processes into account, when relating an observed elevation change to a change in total mass balance of the GrIS. Depending on the assumed density of the volume changes the firn correction decreases the

mass loss of the ice sheet with 33–67 Gt yr^{-1}. This is a reduction of the mass loss of up to 30%, when compared to the direct mass loss estimate from the ICESat measurements without any firn compaction correction.

The error induced by the HIRHAM5 RCM in the firn compaction model is difficult to account for. Further studies have to be conducted to compare the modeled firn densities with in situ measurements before it is possible to estimate the total errors in the firn compaction velocity. Hence, the only error estimate of the firn compaction model is from the error in the linear fit of the inter-annual variability of the firn column. The 2σ are seen in the lower panel of Fig. 4. As seen in the figure the error associated with the firn compaction velocity is most pronounced in coastal areas near large outlet glaciers, where the HIRHAM5 RCM has the largest variability.

The error in the fitted firn compaction velocities will result in an error in the estimate of the total mass loss of the GrIS. The error seen in Fig. 4f has been summed over each of the 5×5 km grid boxes above the ELA, to give the resulting volume error. This volume induced by the error in the fitted firn velocities is then converted into mass by the surface density, resulting in a firn compaction induced error between 14–30 Gt yr^{-1} depending on which ice or firn density is assumed.

6   Additional elevation change corrections

The elevation changes observed by ICESat include signals from processes which do not contribute to the mass balance of the GrIS. The most significant contribution is the firn compaction, but it is also necessary to correct for glacial isostatic adjustment (GIA), elastic uplift caused by the present-day mass changes and the ICESat intercampaign elevation biases.

2123

6.1   Vertical bedrock movement

Elevation changes which are not related to ice volume changes will be detected by ICESat, and these must be removed from the estimated $\frac{dH}{dt}$ values in order to determine the mass balance of the ice sheet. A bedrock movement (w_{br}) caused by GIA and elastic uplift from present-day mass changes will be a part of the elevation changes observed by ICESat.

We use a GIA contribution, according to Peltier (2004). It is based on the ice history model ICE-5G and the VM2 Earth model (http://pmip2.lsce.ipsl.fr/design/ice5g/). The rate of vertical motion caused by GIA is removed from the ICESat $\frac{dH}{dt}$ estimates. We find that this correction contributes to the mass balance of the GrIS with an amount of approximately $+1$ Gt yr^{-1}.

The present-day ice sheet mass changes cause an elastic response of the bedrock (e.g., Khan et al., 2010). These vertical displacements are computed by solving the Sea Level Equation, the fundamental equation that governs the sea level changes associated with glacial isostatic adjustment (Farrell and Clark, 1976). Since the time scale of the mass changes considered here is extremely short compared with the Maxwell relaxation time of the mantle (Spada et al., 2010), any viscoelastic effect is neglected and the ice thickness variations deduced by ICESat are spatially convolved with purely elastic loading "h" Love numbers. Sea level variations associated with melting are computed first, taking into account the elastic response of the Earth and the gravitational interaction between the ice sheets, the oceans and the mantle. Then, vertical displacements are retrieved by the surface load history over the entire surface of the Earth, associated with ice thickness variations and sea level changes. The results in Fig. 5 are obtained from a suitably modified version of the code SELEN 2.9 (Spada and Stocchi, 2007), which solves the Sea Level Equation iteratively, essentially following a variant of the pseudo-spectral method introduced by Mitrovica and Peltier (1991). A maximum harmonic degree $l_{max} = 128$ is used here. Vertical displacement is computed in the reference frame with the origin in the center of mass of the system (Earth+Load), and

2124

includes the harmonic component of degree one (Greff-Lefftz and Legros, 1997). We find that the elastic uplift correction correspond to -4 to $-2\,\mathrm{Gt\,yr^{-1}}$, dependent on the mass loss. The elastic vertical displacement based on the results from method M3 (Sect. 3.3) is shown in Fig. 5.

6.2 ICESat intercampaign bias correction

It has been documented that there are elevation biases between the different ICESat laser campaigns. Following the method described in Gunter et al. (2009), the trend in the ICESat intercampain bias is estimated by (O. B. Andersen and T. Bondo, personal communication, 2010). The GLA15 release 31 ocean altimetry elevations are compared to a mean sea surface topography model (DNSC08). The trend is found to be $1.29 \pm 0.4\,\mathrm{cm\,yr^{-1}}$, when corrected for an assumed actual sea level rise of $0.3\,\mathrm{cm\,yr^{-1}}$ (Leuliette et al., 2004). This trend in intercampaign biases contributes with approximately $14 \pm 4\,\mathrm{Gt\,yr^{-1}}$ to the mass balance.

7 Mass balance of the GrIS

Determining the mass change of the GrIS is a complex problem with multiple solutions, depending on the type of observation and/or the level of theoretical complexity applied to solve the problem. This complexity can explain the different estimates of the total mass balance of the GrIS, which appear in the literature. To summarize the results of our studies, the total mass balance estimates of the GrIS are listed in Table 2. We have chosen to derive the mass change with and without the firn compaction correction of elevation change, to highlight the importance of this correction. The second key assumption in the derivation of the mass loss is ρ, from which the volume change is related to mass. The assumption, that an elevation decrease above the ELA is caused by a loss of glacial ice somewhere in the ablation area by ice dynamics, enhances the estimated mass loss of the GrIS. Therefore, the total mass balances estimates

(Table 2) are derived with and without this remote mass loss of ice. In the calculation without remote ice loss, ρ_s is applied for all elevation changes above the ELA.

Our best estimate of the present total mass balance of the GrIS is $-210 \pm 21\,\mathrm{Gt\,yr^{-1}}$ based on the comprehensive error analysis of the ICESat observations and theoretical treatment of the surface density and firn compaction modelling. The spatial distribution of the mass balance is seen in Fig. 6. This mass loss is equivalent to a global sea level rise of $0.58\,\mathrm{mm\,yr^{-1}}$. The uncertainty estimate on the mass change is obtained from the bootstrap procedure. Each resample is transformed into a mass change estimates according to Sect. 5, hence the 1000 resamples will make up a distribution from which the error is obtained.

The mass loss of the major outlet glaciers is evident in the figure, along with the interior part of the GrIS showing no changes over the period. The western side of the South Greenland ice divide is appearing to gain mass, which may be caused by the increasing precipitation (cf. Fig. 4c). The most prominent area of mass increase is the upper area of the Storstrømmen (Bøggild et al., 1994) outlet glacier in Northeast Greenland. The ice sheet drainage basin ending in Storstrømmen is believed to originate in the central part of the GrIS near the summit area (Rignot and Kanagaratnam, 2006). Therefore, changes in Storstrømmen glacier may be caused by effects inland, or the dynamical response of the GrIS due to changes in climate. However, this has to be verified by additional studies of this area.

8 Discussion and conclusions

Using four different methods to derive elevation changes of the GrIS from ICESat data during the period 2003–2008 reveals a consistent picture of massive ice thinning along the margin of the GrIS and a smaller elevation increase in the interior parts. The thinning is most evident along the southeast and the west coasts. An interpolation and bootstrap approach is applied, in order to derive a total annual vol-

ume change of snow/ice together with uncertainties for all four methods. We find volume changes of $-237 \pm 25 \, \text{km}^3 \, \text{yr}^{-1}$ to $-147 \pm 24 \, \text{km}^3 \, \text{yr}^{-1}$ depending on the method used. We conclude that method 3 is preferable, corresponding to a volume change of $-237 \pm 25 \, \text{km}^3 \, \text{yr}^{-1}$.

In order to correct the observed elevation changes for processes not contributing to the mass balance, we have estimated the firn compaction, vertical bedrock movement caused by GIA and elastic uplift, and the ICESat intercampaign elevation bias.

The firn compaction model is forced by the HIRHAM5 RCM, and we find this correction to be the largest and that it contributes with approximately $+57 \pm 14 \, \text{Gt} \, \text{yr}^{-1}$ to the total mass balance. The trend in the ICESat intercampaign bias is found to be $-1.29 \pm 0.4 \, \text{cm} \, \text{yr}^{-1}$ which corresponds to a mass gain of approximately $14 \pm 4 \, \text{Gt} \, \text{yr}^{-1}$. The elastic uplift of the bedrock, caused by the present-day mass changes are found to contribute with -4 to $-2 \, \text{Gt} \, \text{yr}^{-1}$ to the total mass balance and the GIA correction is $+1 \, \text{Gt} \, \text{yr}^{-1}$.

The firn compaction model can, beside its application shown here, also be used to validate the RCM forcing, by comparing the modelled stratification of the firn with in situ observation from the GrIS. However, a model comparison study of different RCs for the GrIS has not been within the scope of the presented work, but might be elaborated in the future.

Modelled surface densities are used to convert the volume change into mass balance. Based on the preferred method M3, for deriving elevation changes, we estimate a mass balance of the GrIS for 2003–2008 of $-210 \pm 21 \, \text{Gt} \, \text{yr}^{-1}$. This mass loss is equivalent to a global sea level rise of $0.58 \, \text{mm} \, \text{yr}^{-1}$.

This mass balance estimate is in good agreement with results by others. Based on GRACE data, Velicogna (2009) has estimated the mass loss to be $230 \pm 33 \, \text{Gt} \, \text{yr}^{-1}$ during the period 2002–2009, and Wouters et al. (2008) find a mass loss of $179 \pm 25 \, \text{Gt} \, \text{yr}^{-1}$ for the years 2003–2008. van den Broeke et al. (2009) find a total mass balance of $-237 \pm 20 \, \text{Gt} \, \text{yr}^{-1}$ for 2003–2008, from modeled surface mass balance and observed discharge.

2127

Finally, our total mass balance result is large compared to the ICESat derived mass loss of $139 \pm 68 \, \text{Gt} \, \text{yr}^{-1}$ found by Slobbe et al. (2009), based on data from 2003 to 2007. We believe that we have improved the application of ICESat data to estimate the total mass balance of the GrIS, by using a novel approach including firn compaction and density modelling.

References

Abdalati, W., Krabill, W., Frederick, E., Manizade, S., Martin, C., Sonntag, J., Swift, R., Thomas, R., Wright, W., and Yungel, J.: Outlet glacier and margin elevation changes: near-coastal thinning of the Greenland ice sheet, J. Geophys. Res., 106, 33729–33741, doi:10.1029/2001JD900192, 2001. 2105, 2113

Abshire, J. B., Sun, X., Riris, H., Sirota, J. M., McGarry, J. F., Palm, S., Yi, D., and Liiva, P.: Geoscience Laser Altimeter System (GLAS) on the ICESat mission: on-orbit measurement performance, Geophys. Res. Lett., 32, L21S02, doi:10.1029/2005GL024028, 2005. 2107

Benson, C. S.: Stratigraphic Studies in the Snow and Firn of the Greenland Ice Sheet, Tech. Rep. 70, SIPRE (Snow Ice and Permafrost Research Establishment) Research Report, US army corps of engineers, Hanover, New Hampshire, 1962. 2120

Bøggild, C. E.: Preferential flow and melt water retention in cold snow packs in West-Greenland, Nord. Hydrol., 31, 287–300, 2000. 2120

Bøggild, C. E., Reeh, N., and Oerter, H.: Modelling ablation and mass-balance sensitivity to climate change of Storstrømmen, Northeast Greenland, Global Planet. Change, 9, 79–90, doi:10.1016/0921-8181(94)90009-4, 1994. 2126

2128

Box, J. E., Bromwich, D. H., and Bai, L.-S.: Greenland ice sheet surface mass balance 1991–2000: application of Polar MM5 mesoscale model and in situ data, J. Geophys. Res., 109, 16105, doi:10.1029/2003JD004451, 2004. 2121

Christensen, O. B., Drews, M., Christensen, J., Dethloff, K., Ketelsen, K., Hebestadt, I., and Rinke, A.: The HIRHAM regional climate model. Version 5, Tech. Rep. 06-17, DMI technical report, available at: http://www.dmi.dk/dmi/tr06-17.pdf, Cambridge University Press, Cambridge, 2006. 2119

Davies, H. C.: A laterul boundary formulation for multi-level prediction models, Q. J. Roy. Meteor. Soc., 102, 405–418, doi:10.1002/qj.49710243210, 1976. 2119

Davison, A. C. and Hinkley, D.: Bootstrap Methods and their Application, 8th edn., Cambridge Series in Statistical and Probabilistic Mathematics, Meteorological Institute, University of Bonn, Bonn, 2006. 2114

DiMarzio, J., Brenner, A., Schutz, R., Shuman, C., and Zwally, H.: GLAS/ICESat 1 km laser altimetry digital elevation model of Greenland, Digital media, National Snow and Ice Data Center, Boulder, CO, 2007. 2109

Eerola, K.: About the performance of HIRLAM version 7.0, Tech. Rep. 51 Article 14, HIRLAM Newsletter, available at: http://hirlam.org/, Danish Meteorological Institute, Copenhagen, 2006. 2119

Farrell, W. E. and Clark, J. A.: On postglacial sea level, Geophys. J. Roy. Astr. S., 46, 647–667, doi:10.1111/j.1365-246X.1976.tb01252.x, 1976. 2124

Fricker, H. A. and Padman, L.: Ice shelf grounding zone structure from ICESat laser altimetry, Geophys. Res. Lett., 33, L15502, doi:10.1029/2006GL026907, 2006. 2106, 2108

Fricker, H. A., Borsa, A., Minster, B., Carabajal, C., Quinn, K., and Bills, B.: Assessment of ICESat performance at the salar de Uyuni, Bolivia, Geophys. Res. Lett., 32, L21S06, doi:10.1029/2005GL02342, 2005. 2107

Greff-Lefftz, M. and Legros, H.: Some remarks about the degree one deformations of the Earth, Geophys. J. Int., 131, 699–723, doi:10.1111/j.1365-246X.1997.tb06607.x, 1997. 2125

Gunter, B., Urban, T., Riva, R., Helsen, M., Harpold, R., Poole, S., Nagel, P., Schutz, B., and Tapley, B.: A comparison of coincident GRACE and ICESat data over Antarctica, J. Geodesy, 83, 1051–1060, doi:10.1007/s00190-009-0323-4, 2009. 2125

Helsen, M. M., van den Broeke, M. R., van de Wal, R. S. W., van de Berg, W. J., van Meijgaard, E., Davis, C. H., Li, Y., and Goodwin, I.: Elevation changes in Antarctica mainly determined by accumulation variability, Science, 320, 1626–1629, doi:10.1126/science.1153894,

2129

2008. 2116

Herron, M. and Langway, C.: Firn densification: an empirical model, J. Glaciol., 25, 373–385, 1980. 2117, 2118

Howat, I. M., Smith, B. E., Joughin, I., and Scambos, T. A.: Rates of Southeast Greenland ice volume loss from combined ICESat and ASTER observations, Geophys. Res. Lett., 35, L17505, doi:10.1029/2008GL034496, 2008. 2106, 2108, 2111

Jansson, P., Hock, R., and Schneider, T.: The concept of glacier storage: a review, J. Hydrol., 282, 116–129, doi:10.1016/S0022-1694(03)00258-0, 2003. 2120

Joughin, I., Smith, B. E., Howat, I. M., Scambos, T., and Moon, T.: Greenland flow variability from ice-sheet-wide velocity mapping, J. Glaciol., 56, 415–430(16), doi:10.3189/002214310792447734, 2010. 2105

Khan, S. A., Wahr, J., Bevis, M., Velicogna, I., and Kendrick, E.: Spread of ice mass loss into Northwest Greenland observed by GRACE and GPS, Geophys. Res. Lett., 37, L06501, doi:10.1029/2010GL042460, 2010. 2124

Leuliette, E. W., Nerem, R. S., and Mitchum, G. T.: Calibration of TOPEX/Poseidon and Jason altimeter data to construct a continuous record of mean sea level changes, Mar. Geod., 27, 79–94, doi:10.1080/01490410490465193, 2004. 2125

Li, J., Zwally, H. J., Cornejo, H., and Yi, D.: Seasonal variation of snow-surface elevation in North Greenland as modeled and detected by satellite radar altimetry, Ann. Glaciol., 37, 233–238, doi:10.3189/172756403781815889, 2003. 2118

Li, J., Zwally, H. J., and Comiso, J. C.: Ice-sheet elevation changes caused by variations of the firn compaction rate induced by satellite-observed temperature variations (1982–2003), Ann. Glaciol., 46, 8–13, doi:10.3189/172756407782871486, 2007. 2106

Luthcke, S. B., Zwally, H. J., Abdalati, W., Rowlands, D. D., Ray, R. D., Nerem, R. S., Lemoine, F. G., McCarthy, J. J., and Chinn, D. S.: Recent Greenland ice mass loss by drainage system from satellite gravity observations, Science, 314, 1286–1289, doi:10.1126/science.1130776, 2006. 2106

Mitrovica, J. X. and Peltier, W. R.: On post-glacial geoid subsidence over the equatorial ocean, J. Geophys. Res., 96, 20 053–20 071, 1991. 2124

NSIDC: GLAS altimetry product usage guidance, available at: http://nsidc.org/data/docs/daac/glas_altimetry/usage.html, National Snow and Ice data Center, University of Colorado, Boulder, 2010. 2107

Paterson, W. S. B.: Physics of Glaciers, 3rd edn., Butterworth-Heinemann, 3rd edn. 1994,

2130

reprinted with corrections 1998, 2001, 2002, Oxford, 2002. 2116

Pebesma, E. J.: Mapping groundwater quality in The Netherlands, Netherlands Geographical studies, 199, avilable at: http://www.geog.uu.nl/ngs/ngs.html,Utrecht University, Utrecht, 1996. 2114

5   Pebesma, E. J.: Multivariable geostatistics in S: the gstat package, Comput. Geosci., 30, 683–691, doi:10.1016/j.cageo.2004.03.012, 2004. 2114

Peltier, W.: Global glacial isostasy and the surface of the ice-age Earth: the ICE-5G (VM2) model and GRACE, Annu. Rev. Earth Pl. Sc., 32, 111–149, doi:10.1146/annurev.earth.32.082503.144359, 2004. 2124

10 Pritchard, H. D., Arthern, R. J., Vaughan, D. G., and Edwards, L. A.: Extensive dynamic thinning on the margins of the Greenland and Antarctic ice sheets, Nature, 461, 971–975, doi:10.1038/nature08471, 2009. 2106, 2108, 2110, 2113

Reeh, N.: Parameterization of melt rate and surface temperature on the Greenland ice sheet, Polarforschung 1989, 5913, 113–128, 1991. 2120

15 Reeh, N.: A nonsteady-state firn-densification model for the percolation zone of a glacier, J. Geophys. Res., 113, F03023, doi:10.1029/2007JF000746, 2008. 2117, 2118

Reeh, N., Fisher, D. A., Koerner, R. M., and Clausen, H. B.: An empirical firn-densification model comprising ice lenses, Ann. Glaciol., 42, 101–106, doi:10.3189/172756405781812871 http://www.ingentaconnect.com/content/igsoc/agl/2005/
20 00000042/00000001/art00017, 2005. 2117, 2121

Rignot, E. and Kanagaratnam, P.: Changes in the velocity structure of the Greenland ice sheet, Science, 311, 986–990, doi:10.1126/science.1121381, 2006. 2105, 2126

Rignot, E., Braaten, D., Gogineni, S. P., Krabill, W. B., and McConnell, J. R.: Rapid ice discharge from Southeast Greenland glaciers, Geophys. Res. Lett., 31, L10401,
25 doi:10.1029/2004GL019474, 2004. 2105

Roeckner, E., Bauml, G., Bonaventura, L., Brokopf, R., Esch, M., Giorgetta, M., Hagemann, S., Kirchner, I., Kornblueh, L., Manzini, E., Rhodin, A., Schlese, U., Schulzweida, U., and Tompkins, A.: The atmospheric general circulation model ECHAM 5. Part I: model description, Tech. Rep. 349, Max-Planck-Institute for Meteorology, Hamburg, 2003. 2119

30 Simmons, A., Uppala, S., Dee, D., and Kobayashi, S.: ERA-interim: new ECMWF reanalysis products from 1989 onwards, ECMWF Newsletter, 110, 25–35, 2007. 2119

Slobbe, D., Lindenbergh, R., and Ditmar, P.: Estimation of volume change rates of Greenland's ice sheet from ICESat data using overlapping footprints, Remote Sens. Environ., 112, 4204–

4213, doi:10.1016/j.rse.2008.07.004, 2008. 2106, 2108, 2109, 2113

Slobbe, D., Ditmar, P., and Lindenbergh, R.: Estimating the rates of mass change, ice volume change and snow volume change in Greenland from ICESat and GRACE data, Geophys. J. Int., 176, 95–106, doi:10.1111/j.1365-246X.2008.03978.x, 2009. 2128

5   Smith, B. E., Bentley, C. R., and Raymond, C. F.: Recent elevation changes on the ice streams and ridges of the Ross Embayment from ICESat crossovers, Geophys. Res. Lett., 32, L21S09, doi:doi:10.1029/2005GL024365, 2005. 2107

Smith, B. E., Fricker, H. A., Joughin, I. R., and Tulaczyk, S.: An inventory of active subglacial lakes in Antarctica detected by ICESat (2003-2008), J. Glaciol., 55, L21S09, 2009. 2111

10 Sørensen, L. S. and Forsberg, R.: Greenland ice sheet mass loss from GRACE monthly models, Gravity Geoid Earth Observ., 135, 527–532, doi:10.1007/978-3-642-10634-7_70, 2010. 2106

Spada, G. and Stocchi, P.: SELEN: a Fortran 90 program for solving the "Sea Level Equation", Comput. Geosci., 33(4), 538–562, doi:10.1016/j.cageo.2006.08.006., 2007. 2124

15 Spada, G., Colleoni, F., and Ruggieri, G.: Shallow upper mantle rheology and secular ice sheets fluctuations, Tectonophysics, doi:10.1016/j.tecto.2009.12.020, 2010. 2124

Thomas, R., Davis, C., Frederick, E., Krabill, W., Li, Y., Manizade, S., and Martin, C.: A comparison of Greenland ice-sheet volume changes derived from altimetry measurements, J. Glaciol., 54, 203–212, doi:10.3189/002214308784886225, 2008. 2113

20 Thomas, R., Frederick, E., Krabill, W., Manizade, S., and Martin, C.: Recent changes on Greenland outlet glaciers, J. Glaciol., 55, 147–162, doi:10.3189/002214309788608958, 2009. 2113

van den Broeke, M., Bamber, J., Ettema, J., Rignot, E., Schrama, E., van de Berg, W. J., van Meijgaard, E., Velicogna, I., and Wouters, B.: Partitioning recent greenland mass loss,
25 Science, 326, 984–986, doi:10.1126/science.1178176, 2009. 2106, 2127

Velicogna, I.: Increasing rates of ice mass loss from the Greenland and Antarctic ice sheets revealed by GRACE, Geophys. Res. Lett., 36, L19503, doi:10.1029/2009GL040222, 2009. 2127

Velicogna, I. and Wahr, J.: Greenland mass balance from GRACE, Geophys. Res. Lett., 32,
30 L18505, doi:10.1029/2005GL023955, 2005. 2106

Wouters, B., Chambers, D., and Schrama, E. J. O.: GRACE observes small-scale mass loss in Greenland, Geophys. Res. Lett., 35, L20501, doi:10.1029/2008GL034816, 2008. 2106, 2127

Wu, X., Heflin, M., Schotman, H., Vermeersen, B., Dong, D., Gross, R., Ivins, E., Moore, A., and Owen, S.: Simultaneous estimation of global present-day water transport and glacial isostatic adjustment, Nat. Geosci., 3, 642–646, doi:10.1038/ngeo938, 2010. 2106

Zwally, H., Schutz, R., Bentley, C., Bufton, J., Herring, T., Minster, J., Spinhirne, J., and Thomas, R.: GLAS/ICESat L2 Antarctic and Greenland ice sheet altimetry data V031, National Snow and Ice Data Center, Boulder, CO, avilable at: http://nsidc.org/data/gla12.html, 2010. 2107

Zwally, H. J. and Li, J.: Seasonal and interannual variations of firn densification and ice-sheet surface elevation at the Greenland summit, J. Glaciol., 48, 199–207, doi:10.3189/172756502781831403, 2002. 2116, 2117, 2118

Table 1. ICESat data description. Shown is the laser campaign identifier (ID), data release number (RL), and time span of the campaigns. N and M are the number of measurements from the GrIS before and after the data culling, respectively.

ID	RL	Time span	N	M
L2A	531	4 Oct 2003–18 Nov 2003	1 095 647	941 052
L2B	531	17 Feb 2004–20 Mar 2004	815 998	695 242
L2C	531	18 May 2004–20 Jun 2004	739 672	680 031
L3A	531	3 Oct 2004–8 Nov 2004	851 789	727 425
L3B	531	17 Feb 2005–24 Mar 2005	829 689	704 680
L3C	531	20 May 2005–22 Jun 2005	800 876	679 827
L3D	531	21 Oct 2005–23 Nov 2005	821 825	695 949
L3E	531	22 Feb 2006–27 Mar 2006	883 492	752 123
L3F	531	24 May 2006–25 Jun 2003	743 702	626 463
L3G	531	25 Oct 2006–27 Nov 2003	809 655	698 710
L3H	531	12 Mar 2007–14 Apr 2007	838 647	778 350
L3I	531	2 Oct 2007–4 Nov 2007	761 576	705 639
L3J	531	17 Feb 2008–21 Mar 2008	375 239	368 148
Total			10 367 807	9 053 639

Table 2. The total mass balance the GrIS estimated based on the different methods of ICESat processing and assumptions in the firn compaction modelling. The contribution to the total mass balance above and below the ELA is specified, along with the total mass balance above an altitude of 2000 m. The error estimate from the firn compaction modelling is derived only for the full firn correction. Note that the mass balance below the ELA is unaffected by firn model processes and is therefore the same for all firn assumptions.

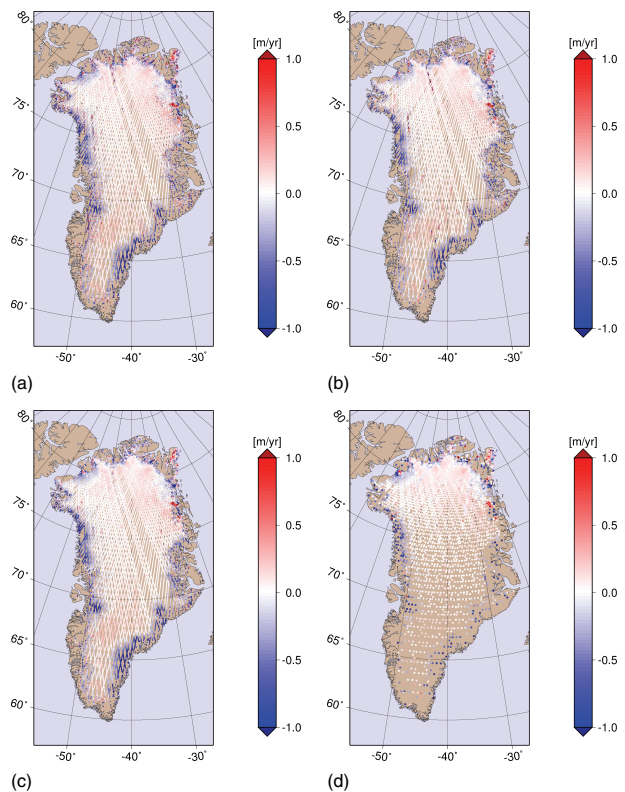|	ICESat Volume [km^3 yr^{-1}]	With remote removal of ice			Below ELA [Gt yr^{-1}]	Without remote removal of ice		
		Total [Gt yr^{-1}]	Above ELA [Gt yr^{-1}]	Above 2000 m [Gt yr^{-1}]		Total [Gt yr^{-1}]	Above ELA [Gt yr^{-1}]	Above 2000 m [Gt yr^{-1}]
With firn correction								
M1	-225 ± 23	-199 ± 20	-72	-7	-127	-157	-30	$+6$
M2	-179 ± 15	-155 ± 12	-54	-5	-101	-121	-20	$+7$
M3	-237 ± 25	-210 ± 21	-77	-8	-133	-166	-33	$+5$
M4	-147 ± 24	-118 ± 21	-40	-9	-78	-92	-14	$+2$
Without firn correction								
M1	-225	-256	-129	-28	-127	-190	-63	-5
M2	-179	-212	-111	-25	-101	-154	-53	-4
M3	-237	-267	-134	-29	-133	-199	-66	-5
M4	-147	-177	-99	-31	-78	-126	-48	-9

Fig. 1. Elevation changes derived from ICESat data using 4 different methods. **(a)** M1, **(b)** M2, **(c)** M3, and **(d)** M4.
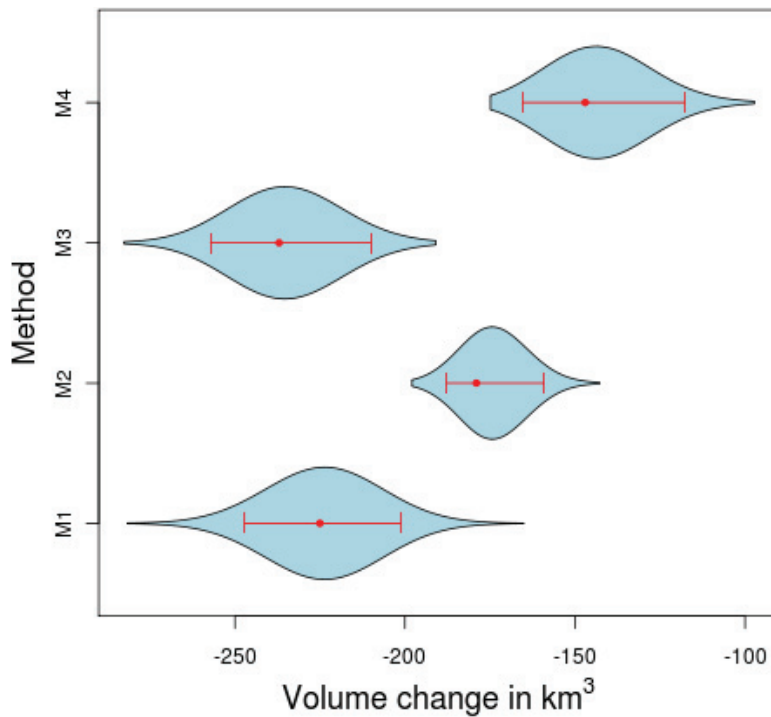
Fig. 2. Violin plot of the 4 method results. The blue area indicates the distribution of 1000 bootstrap samples. The red dots are the point estimates of volume change, and the red bars indicate the 95% confidence interval.

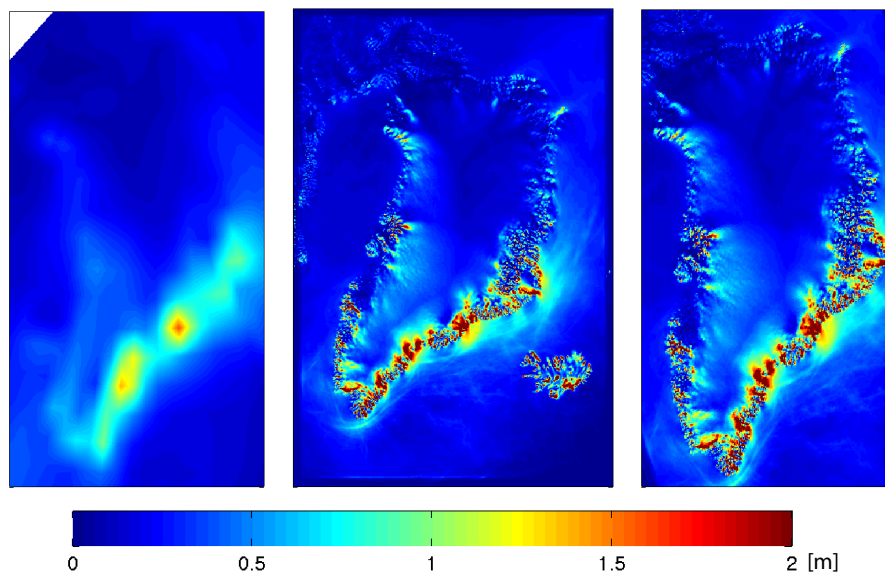**Fig. 3.** The 2008 snowfall on a scale at 0 to 2 m of water equivalent (from blue to red). (Left) The ERA-Interim $1.5° \times 1.5°$ resolution linear interpolated onto the equal distance 5 km × 5 km grid. (Middle) The regional HIRHAM5 dynamical downscaling of the ERA-Interim. HIRHAM5 applies a rotated map projection, with a grid spacing of $0.05° \times 0.05°$. This projection gives a metric resolution of ~5.5 km × 5.5 km. (Right) Nearest neighbor interpolation of the HIRHAM5 onto the equal distance 5 km × 5 km grid. The highly dynamic behavior of the precipitation from the HIRHAM5 model is preserved in the transformation of the map projections.
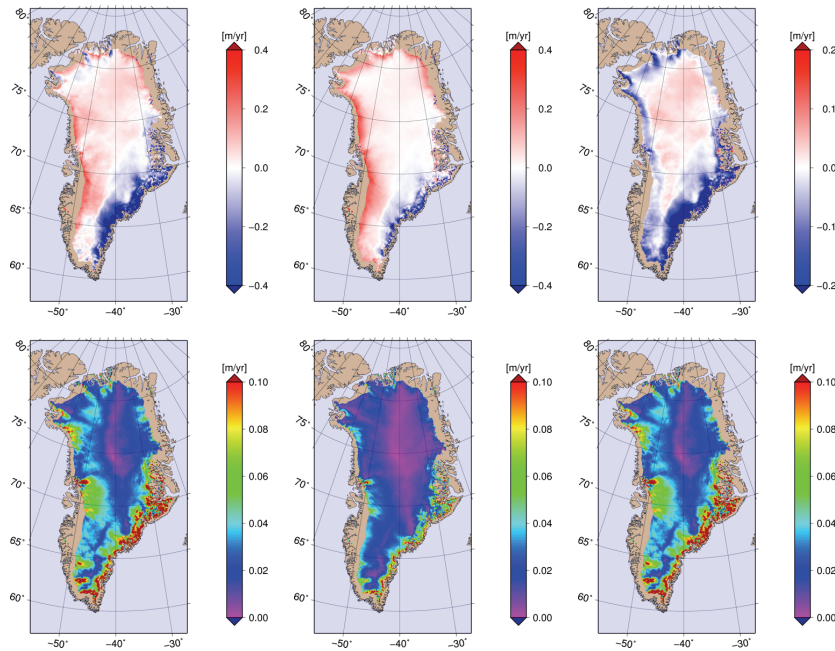
Fig. 4. The different contributions to the the firn compaction modelling for the period from 2003 to 2008, forced by the HIRHAM5 climatology. Only the area above the ELA is shown in the figure. The upper panels show the modeled firn process, estimated from a linear fit for the period 2003 to 2008. **(a)** The modeled change in the thickness of the top 15 annual firn layers. **(b)** The change of ice equivalent thickness of the top 15 annual firn layers. **(c)** The change in air volume in the top firn, which is equivalent to the firn compaction velocity defined in Eq. (11). The work flow of the computations is (c) = (a − b). **(d)**, **(e)** and **(f)** show the 2σ standard deviation of the linear trend in (a), (b) and (c), respectively.
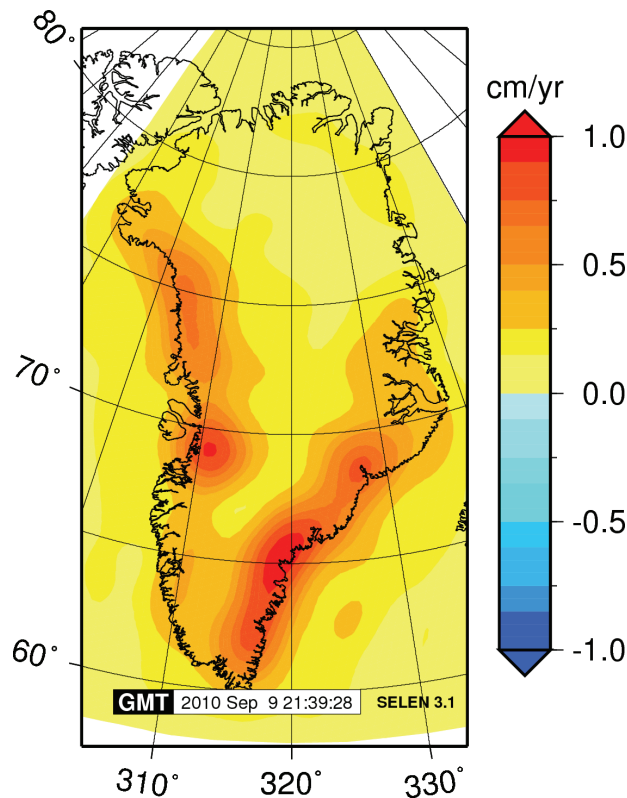
Fig. 5. Elastic vertical displacement caused by present-day mass changes in Greenland, referred to the period of one year, computed according to mass changes obtained by M3.
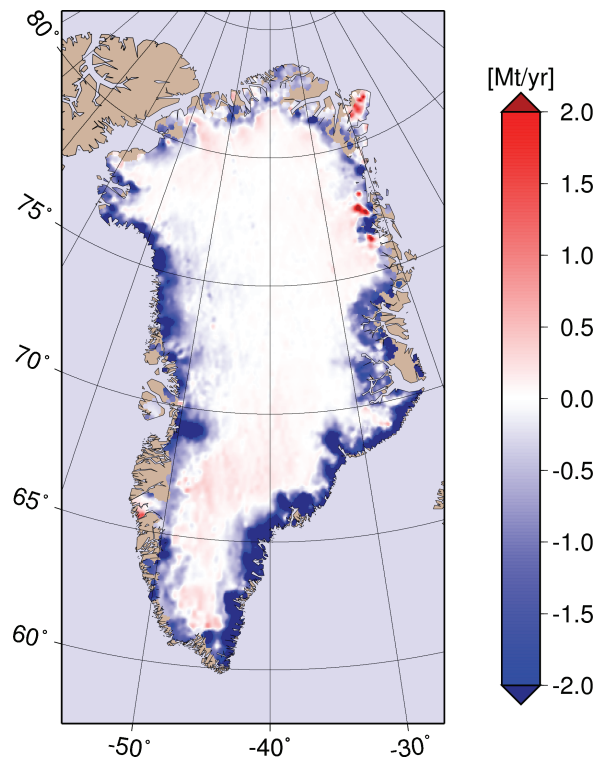
Fig. 6. The yearly spatial distribution of the mass change of the GrIS, derived for each of the grid cells. The result is based on the estimate derived by M3. The pattern of coastal thinning seen in Fig. 1 is also found in the mass change of the GrIS.